Se si ivity of ~ i-Angle Remote Sensing O s va i is t Aerosol Sphericity

Ralph Kahn, Robe West Duncan McDonald and B a n Rheingans

Jet Propulsion aboratory California nstitute of Technology

4800 Oak Grove ive Pasadena CA 91 09

an d ~ ichael Mishchenko

NASA Goddard nstitute for Space Studies, New Y ork NY 025

For The Journal of Geophysical Research, Atmospheres
Special Issue on Aerosol Remote Sensing

ece ber 28, 1995

last revised: 12/27/95

Abstract

Multi-angle, multi-spectral remote sensing observations, such as those anticipated from the Earth Observing System (EOS) Multi-angle Imaging SpectroRadiometer (MISR), can distinguish spherical from non spherical particles over *calm ocean* for mineral-dust-like particles with the range of sizes and column amounts expected under natural conditions. The ability to make such distinctions is critical if remote sensing of atmospheric aerosol properties is to provide significant new contributions to our understanding of the global-scale, clear-sky solar radiation balance. According to theoretical simulations, the measurements can retrieve column optical depth for non-spherical particles to an accuracy of at least 0.05 or 10%, whichever is larger. In addition, three to four distinct size groups between 0.1 and 2.0 microns effective radius can be identified at most latitudes.

1. Introduction

In a recent paper, *Mishchenko et al.* [1995] studied the implications of assuming spherical particles in the retrieval of aerosol properties from remote sensing data, when non-spherical particles are present in the atmosphere. They demonstrate that for observations of dust-like aerosols over ocean, if a retrieval of total column optical depth is performed based on an assumption of spherical particles when in fact the particles are non-spherical, the results can be seriously in error. For the cases studied, the systematic error in total column optical depth is very sensitive to the geometry of the observation, and can be arbitrarily large, when simulated monospectral satellite measurements at a single emission angle are used in the retrieval, even assuming noiseless data.

The systematic errors demonstrated by *Mishchenko et al.* [1995] are unacceptably large for climate change studies. The magnitude of direct radiative effects from atmospheric aerosols is as yet uncertain, but it may be comparable to the size of the anticipated incremental greenhouse warming due to a doubling of atmospheric CO_2 [*Andreae*, 1994; *Penner et al.*, 1994; *Kiehl and Briegleb*, 1993; *Charlson et al.*, 1992; *Hansen and Lacis*, 1990]. Dust-like particles, which are likely to be non-spherical, make important contributions to the optical depth over large regions of the planet [*Tegen and Fung*, 1994].

Currently, satellite-based remote sensing instruments provide our best hope of obtaining the spatial and temporal coverage required for global monitoring of atmospheric aerosols. Although the only global-scale satellite-based retrieval of total column aerosol optical depth now in routine operation relies on a single channel of AVHRR data [*Rao et al.*, 1989; *Husar and Stowe*, 1994], new satellite remote sensing instruments with *multi-angle* and multi-spectral capabilities are being built. We present in this paper a theoretical study of the ability of multi-angle and multi-spectral remote sensing techniques to distinguish between spherical and non spherical particles. This study is part of our program to characterize the performance of the Multi-angle Imaging SpectroRadiometer (MISR) instrument, which is scheduled for launch into polar orbit on the EOS-AM1 platform in June, 1998 [*Diner et al.*, 1991].

The MISR instrument will measure the upwelling visible radiance from Earth in 4 spectral bands centered at 443, 550, 670, and 865 nm, at each of 9 emission angles spread out in the forward and aft directions along the flight path at $\pm 70.5°$, $\pm 60.0°$, $\pm 45.6°$, $\pm 26.1°$, and nadir. The spatial sampling rate is 275 meters in the cross track direction at all angles. Over a period of 7 minutes, a 360 km wide swath of Earth comes into the view of the cameras at each of the 9 emission angles, providing a wide range of scattering angle coverage for each surface location. The data will be used to characterize aerosol optical depth, aerosol type, surface albedo and bi-directional reflectance, and cloud properties. Global coverage will be acquired about once in 9 days at the equator; the nominal mission lifetime is 6 years.

2. Modeling the Observations

For this study, we use single scattering phase functions and albedos for spherical and non-spherical particles similar to those generated by *Mishchenko et al.* [1995]. The non-spherical particles are modeled as a mixture of polydisperse prolate and oblate spheroids with a uniform distribution of aspect ratios ranging between 1.2 and 2.4. Both spherical and non-spherical particle sizes are given by power law distributions, with $n(r) = C$ for $r \leq r_1$, $n(r) = C(r_1/r)^3$ for $r_1 \leq r \leq r_2$, and $n(r) = 0$ for $r > r_2$. Here r is the particle radius for spherical particles and the radius of a sphere with equal surface area for non-spherical particles. C is a normalization constant for the distribution. r_1 and r_2 are parameters, selected so that the cross-section mean weighted radius of the distribution as a whole is r_{eff}, and the variance of the distribution is v_{eff} [*Mishchenko and Travis*, 1994]. For all cases, v_{eff} is 0.2 and the particle index of refraction is $1.53 - 0.008i$, independent of wavelength. The wavelength dependence of single scattering properties scales as x, where $x = 2\pi r/\lambda$, and λ is the wavelength [*Hansen and Travis*, 1978]. Unless specified otherwise, optical properties presented in this paper are for MISR Band 3 (670 nm); in the underlying calculations, optical properties are properly scaled to account for wavelength dependence in each of the MISR bands used.

Figure 1 compares the single scattering phase functions for distributions of spherical and non-spherical particles of several effective sizes. For the smallest particles, $r_{eff} = 0.05$ µm, which is typical of "nucleation mode" aerosols in the atmosphere, but smaller than common atmospheric mineral dust aerosol distributions. The single scattering phase functions for spherical and non-spherical particles at these sizes are indistinguishable. Distributions with effective radii in the 0.5-to-10 µm range are typical of suspended atmospheric mineral dust aerosols [e.g., *Tegen and Fung*, 1994]. For these larger aerosols, the non-spherical particles put a smaller fraction of the total scattering into the back-scattering direction at scattering angles greater than about 150°, and a larger fraction into the scattering angles between about 100° and 150°, compared to spherical particles with equivalent surface area. The characteristics shown in Figure 1 have been reproduced for other types of randomly-oriented aggregates of non-spherical particles [e.g., *Takano and Liou*, 1989].

The optical properties given by *Mishchenko et al.* [1995] allow us to treat particles with sizes up to about 2 µm, which is adequate to cover the transition in single scattering characteristics between particles with x values in the small (Rayleigh) and large (geometric optics) regimes. Qualitatively, the results for the largest particles we can treat also apply to particles with effective radii between 2 and 10 µm. Quantitative treatment of the sensitivity of multi-angle remote sensing to the larger particles requires additional calculations that are currently underway.

The scattering angle coverage for each of the 9 MISR cameras, as a function of latitude and location in the scan line, is shown in Figure 2 for March 21, for the nominal EOS-AM1 platform orbit. In midlatitudes, scattering angles between about 60° and 160° are covered by the 9 cameras, whereas at high latitudes the range is approximately 40° to 150°, and at low latitudes, 100° to 160°. With changing seasons, the pattern of coverage remains nearly the same, but shifts toward the summer pole.

The MISR Team has developed a radiative transfer code, based on the adding-doubling method [*Hansen and Travis*, 1974], to simulate top-of-atmosphere reflectances as would be observed by the MISR instrument, for arbitrary choice of aerosol type and amount, and variable surface reflectance properties [*Diner et al.*, 1994]. For the present study we have simulated MISR measurements over a Fresnel-reflecting calm ocean surface, in a cloud-free, Rayleigh scattering atmosphere with a surface pressure of 1.013 bar and a standard midlatitude temperature profile. A layer containing either non-spherical or spherical particles is placed between the gas component and the surface. (Sensitivity studies show that for the range of aerosol optical depth treated here, the results would be unaffected if the aerosols were modeled as mixed with the gas in the lowest part of the atmosphere.) The goal is to determine the degree to which we can distinguish between the non-spherical and spherical particle cases from the measurements.

As a measure of instrument sensitivity, we use a normalized χ^2 parameter that weights the contributions from each observed reflectance according to the slant path of the observation through the atmosphere. [In this paper, reflectance is defined as the radiance multiplied by π, and divided by the exo-atmospheric solar irradiance at normal incidence.] A way to define χ^2 that emphasizes the camera-to-camera geometric differences is to divide each spectral measurement by the corresponding spectral measurement in the nadir camera:

$$\chi^2_{geom} = \frac{1}{N\langle m_k \rangle} \sum_{l=1}^{4} \sum_{\substack{k=1 \\ k \neq nadir}}^{9} \frac{m_k \left| \frac{L_{meas}(l,k)}{L_{meas}(l,nadir)} - \frac{L_{comp}(l,k)}{L_{comp}(l,nadir)} \right|}{\sigma^2_{geom}(l,k)} \tag{1}$$

where L_{meas} is the simulated "measured" reflectance, L_{comp} is the simulated reflectance for the "assumed" comparison model, l and k are the indices for wavelength band and camera, N is the number of measurements included in the calculation, m_k are weights, chosen to be the inverse of the cosine of the emission angle appropriate to each camera k, $\langle m_k \rangle$ is the average of weights for all the measurements included in the calculation, and σ_{geom} (a dimensionless quantity) is the uncertainty in the measured channel-to channel reflectance ratio, given by:

$$\sigma^2_{geom}(l,k) = \frac{\sigma^2_{rel}(l,k)}{L^2_{meas}(l,nadir)} + \frac{L^2_{meas}(l,k)\ \sigma^2_{rel}(l,k)}{L^4_{meas}(l,nadir)} \tag{2}$$

where σ_{rel} has units of reflectance and is the relative calibration uncertainty in the reflectance for band l and camera k. For the MISR instrument, the value of σ_{rel} is specified to fall between 0.01 for a target with reflectance of 100%, and 0.02 for a reflectance of 5%, in all channels [*Diner et al.*, 1994]. For these simulations, we model σ_{rel} as varying linearly with reflectance. Note that σ_{rel} includes the effects of systematic calibration errors for ratios of reflectance between channels. Random error due to instrument noise is negligible, based on the high signal-to noise ratio demonstrated during MISR camera testing.

Since the χ^2 parameter is normalized to the number of channels used, a value less than or about unity implies that the comparison model is indistinguishable from the measurements. Values larger than about 5 imply that the comparison model is not consistent with the observations. To illustrate this in subsequent figures, we have developed a color bar with 3 segments: a logarithmic segment for values between 10^{-5} and 1 depicted in shades of blue, a logarithmic segment for values between 5 and 10^4 depicted in shades of red, and a linear segment shown in light green, yellow, and orange shades for the intermediate values. Thus, red shades in the figures indicate situations where the model is clearly distinguishable from the measurement, whereas blue shades indicate that the model is indistinguishable from the measurement. Black is reserved for exact agreement between model and measurement, which can occur in this study because we are working with simulated observations. Note that the color table has been designed so that if these figures are photocopied in black and white, first-order information about the ability to distinguish among models is preserved.

3. Sensitivity of Multi-Angle Multi-Spectral Radiances to Particle Sphericity

In Figure 3A we address the question: If the atmosphere contains non-spherical particles with aerosol optical depth $\tau_{a,atm}$ and distribution of particles with effective radius r_{atm}, could a retrieval with MISR-like multi-spectral, multi-angle data mistakenly interpret the measured reflectances as being due to spherical particles with effective radius r_{comp} and aerosol optical depth $\tau_{a,comp}$?

For aerosol retrievals over ocean, the standard MISR algorithm uses data from all 9 emission angles, but only in the two spectral bands at which the ocean surface is darkest (670 and 865 nm). Simulations were performed for an atmosphere containing non-spherical particles with r_{atm} values of 0.1, 0.5, 1.0, and 2.0 μm, and $\tau_{a,atm}$ values at 670 nm of 0.05, 0.2, and 0.8. Appropriate scaling was used to simulate the data at 865 nm, assuming the particle index of refraction is independent of wavelength.

χ^2_{geom} was then calculated for comparison models that assume distributions of spherical particles with column optical depth $\tau_{a,comp}$ ranging from 0.05 to 1.0 in increments of 0.05, and effective radii r_{comp} ranging from 0.1 to 2.0 μm, in increments of 0.1. According to Figure 3A, the χ^2_{geom} criterion is able to distinguish spherical from non-spherical particles for all cases chosen, except when the atmospheric particles are very small and $\tau_{a,atm}$ is low. We expect no discrimination for very small particles, since the corresponding spherical and non-spherical single scattering phase functions are indistinguishable (Figure 1). Note that even for the very small particle case, the only acceptable value of r_{comp} is the corresponding equivalent-sphere radii for r_{atm}, and the acceptable $\tau_{a,comp}$ values are within 0.05 of the corresponding values of $\tau_{a,atm}$.

Figure 3B tests the converse situation: non-spherical particles are assumed for the comparison models when the atmosphere actually contains spherical particles. Here again the only case where the difference in particle shape would not be detected is when the atmospheric particles are very small and $\tau_{a,atm}$ is low.

In addition, for very low atmospheric optical depth, some cases produce two local minima in χ^2_{geom} (though not low enough to qualify as acceptable matches). For the r_{atm}= 0.5 case, the minima occur when r_{comp} is between 0.4 and 1.0 μm. These minima arise because the single scattering albedo for the comparison (spherical) particles is slightly smaller than the corresponding value for non-spherical particles. As the comparison model optical depth is increased, the comparison model reflectance at the scattering angles measured by the instrument (60° to 150°) also increases (Figure 1). For some intermediate value, the difference in reflectance between the spherical and non-spherical cases reaches a local minimum. The absolute minimum, and therefore the best-fit optical depth, still falls at the correct value. As comparison model optical depth increases further, the distinguishability becomes greater.

Similar results are obtained at poleward geometries. At low latitudes the range of scattering angle covered by MISR is diminished. Within about 20° of the subsolar latitude, the scattering angle coverage only extends from 100° to 160° (Figure 2), limiting the sensitivity of the retrieval. This is particularly apparent for both the low optical depth and the small particle size cases, where the reflectance differences between spherical and non-spherical particles are small to begin with. For the smallest particle sizes tested, the retrieval is insensitive to particle shape at low latitudes. For low optical depth, the retrieval is insensitive to particle size and shape at these latitudes, but the retrieved optical depth is still within 0.05 of the correct value.

In Figure 4A we examine the ability of MISR-like measurements to correctly retrieve the properties of non-spherical particles. For this figure, both the atmosphere and comparison models contain non-spherical particles. There are regions of acceptable matches for all cases, with exact agreement when the comparison model parameters equal those of the atmosphere. For low atmospheric optical depth and mid-to-large sized atmospheric particles, a range of sizes satisfies the test. The size discrimination improves with increasing atmospheric optical depth particularly for mid-sized particles.

The optical depth uncertainty is within 0.05 for small and 10% for larger particle sizes, but is close to 50% for the worst case in Figure 4A. By using χ^2_{geom} alone, we have reduced 18 measurements to a single statistic. χ^2_{geom} emphasizes the geometric properties of the scattering, which depend heavily on particle size and shape. However, there is more information in the measurements that may be used to improve the retrieval discrimination ability. For example, we define a statistic that weights the contributions from each observed absolute reflectance according to the slant path through the atmosphere of the observation:

$$\chi^2_{abs} = \frac{1}{N\langle m_k\rangle} \sum_{l=1}^{4} \sum_{k=1}^{9} \frac{m_k \left[L_{meas}(l,k) - L_{comp}(l,k)\right]^2}{\sigma^2_{abs}(l,k)} \qquad (3)$$

where σ_{abs} is the absolute measurement error in the reflectance. (σ_{abs} is nominally three times the corresponding value of σ_{rel} for the MISR instrument [*Diner et al.*, 1994].) This statistic emphasizes the absolute reflectance, which depends heavily on optical depth. Figure 4B shows χ^2_{abs} for the same parameter space covered by χ^2_{geom} in Figure 4A. To fully use the additional information, a model must satisfy *both* χ^2 criteria. This increases the retrieval sensitivity to optical depth to 10% or better over the entire parameter space. Combining the tests also improves slightly the retrieval sensitivity to particle size for larger particles. Size discrimination is poorest for low optical depth. Very similar results in terms of sensitivity to both optical depth and particle size are obtained at higher as well as lower latitudes.

4. Conclusions

Multi-angle, multi-spectral measurements such as those anticipated from the EOS MISR instrument are sensitive to the characteristics of single scattering phase functions that distinguish spherical from non-spherical particles. Simulated mixtures of non-spherical particles covering the range of size distributions and column abundances typical of atmospheric mineral dust over ocean were used, with indices of refraction representative of Sahara dust aerosol samples. A simple χ^2 test is adequate to identify non-spherical particles for all cases except the smallest particles, which have effective radii of 0.1 microns or less, and for low aerosol optical depths at latitudes within about 20° of the subsolar latitude. For the small particle cases, the scattering properties themselves are indistinguishable from those of equivalent spheres.

According to theoretical simulations, MISR-type measurements can retrieve column optical depth for non-spherical particles over calm ocean to an accuracy of at least 0.05 or 10%, whichever is larger. This is true even for cases where particle shape or size is not well-constrained by the retrieval. Two χ^2 tests, one which emphasizes the geometric information in the measurement set, and one which emphasizes the absolute reflectances, are needed to produce these constraints. Constraints on effective radius vary with column optical depth and with the nature of the tests used for the retrieval. With the two χ^2 tests adopted for this study, three to four distinct size groups between 0.1 and 2.0 microns effective radius are distinguishable over the assumed range of column optical depths.

Characterization of the sensitivity of MISR aerosol retrievals for a range of particle compositions and environmental conditions, and refinement of the criteria used for choosing "best-fit" models, are part of continuing work. The MISR Team is currently performing sensitivity studies for aerosol column optical depth, aerosol size distribution, aerosol indices of refraction, aerosol hydration state, mixing of particle types, effects of thin cirrus, fogs, stratospheric aerosols, and underlying surface type.

Acknowledgments. We thank our colleagues D. Diner and J. Martonchik for many discussions of these topics. This research is performed at the Jet Propulsion Laboratory, California Institute of Technology, under contract with the National Aeronautics and Space Administration, and by the NASA Goddard Institute for Space Studies.

Refer('11('('s

Andreae, M.O., Climatic effects of changing atmospheric aerosol levels, in A. Henderson-Sellers, ed., World Survey of Climatology, V.16: *Future Climates of the World*, preprint, 1994.

Charlson, R.J., S. Schwartz, J. Hales, R. Cess, J. Coakley, Jr., J. Hansen, and D. Hofmann, Climate forcing by anthropogenic aerosols, *Science 255*, 423-430, 1992.

Diner, D. J., C.J. Bruegge, J.V. Martonchik, G. W. Bothwell, E.D. Danielson, E. L. Floyd, V.G. Ford, L.E. Hovland, K.L. Jones, and M.L. White, A Multi-angle Imaging SpectroRadiometer for terrestrial remote sensing from the Earth Observing System, *Internat. J. Imaging Systems and 7'(('}/)/01.* 3, 92- 10"/, 1991.

Diner, J., W. Abdou, T. Ackerman, J. Conel, H. Gordon, R. Kahn, J. Martonchik, S. Paradise, M. Wang, and R. West, MISR Level 2 Algorithm Theoretical Basis: Aerosol/Surface Product Part 1 (Aerosol Parameters), JPL D11400, Rev. A, 1994.

Hansen, J., and A. Lacis, Sun and dust versus greenhouse gases: An assessment of their relative roles in global climate change, *Nature 346*, 713-719, 1990.

Hansen, J.E., and L.D. Travis, Light scattering in planetary atmospheres, *Space Sci. Rev. 16*, 527-610, 1974.

Husar, 1<.11., and 1.J.. Stowe, Tropospheric aerosols over the oceans, submitted to *Science*, 199L4.

Kiehl, J.T., and B.P. Briegleb, The relative roles of sulfate aerosols and greenhouse gases in climate forcing, *Science 260*, 311-314, 1993.

Mishchenko, M.I., A.A. Lacis, B.E. Carlson, and L.D. Travis, Nonsphericity of dust-like tropospheric aerosols: implications for aerosol remote sensing and climate modeling, *Geoph. Res. Lett.22*, 1077-1080, 1995.

Mishchenko, M.I., and L.D. Travis, Light scattering by polydisperse, rotationally symmetric nonspherical particles: Linear polarization, *J. Quant. Spectrosc. Radiat. Transfer 51*, 759-778, 1994.

Penner, J.E., R.J. Charlson, J.M. Hales, N.S. 1aulainen, R. 1eifer, '1'. Novakov, J. Ogren, L.F. Radke, S.E. Schwartz, and 1.. Travis, Quantifying and minimizing uncertainty of climate forcing by anthropogenic aerosols, *Bul. Am. Meteoro. ,$'0(.* 75, 375-400, 1994.

Rao, C.R.N., L.L. Stowe, and E.P. McClain, Remote sensing of aerosols over the oceans using AVHRR data: Theory, practice and applications, *Int. J. Remote Sensing 10*, 743-749, 1989.

Takano, Y., and K-N Liou, Solar radiative transfer in cirrus clouds. Part I: Single-scattering properties of hexagonal ice crystals, *J. Atmosph. Sci. 46*, 3-19, 1989.

Tegen, I., and I. Fung, Modeling of mineral dust in the atmosphere: Sources, transport, and optical thickness, *J. Geophys. Res. 99*, 22897-22914, 1994.

Figure Captions

Figure 1. Single scattering phase functions for several pairs of spherical and non-spherical particles with the same values of r_{eff}. For all cases, v_{eff} = 0.2, and λ is 670 nm. (A) r_{eff} = 0.05 µm (Note that the non-spherical case is hidden by the spherical case for this size particle); r_{eff} = 0.1 µm; and r_{eff} = 0.5 µm, (B) r_{eff} = 1.0 µm; and r_{eff} = 2.0 µm.

Figure 2. Range of scattering angles to be sampled by the 9 MISR cameras, as functions of latitude and location in the instrument scan line, for March 21 and the nominal EOS-AM Platform orbit. Sampling extends to 82° latitude, and in some seasons folds over toward 60° in the opposing hemisphere. The pattern remains nearly the same, but shifts poleward, as the solstice seasons approach.

Figure 3. Tests of the ability to distinguish spherical from non-spherical aerosols. (A) For each panel, simulated MISR reflectances were produced for an atmosphere containing non-spherical particles with the specified r_{atm} and $\tau_{a,atm}$. $\tau_{a,atm}$ increases to the right from panel to panel, whereas $r_{eff,atm}$ increases from panel to panel toward the top of the figure. χ^2_{geom} was then calculated using the two longest wavelength MISR channels in all 9 cameras, for comparison models that assume distributions of spherical particles with effective radii r_{comp} and column aerosol optical depth τ_{comp}. All simulations presented are for mid-latitude geometry over a Fresnel-reflecting, calm ocean surface, and include a standard Rayleigh scattering contribution. Colors indicating the value of χ^2_{geom} are plotted in each panel, with r_{comp} increasing toward the top of each plot and τ_{comp} increasing to the right. (B) Same as Figure 3A, except that the atmosphere is assumed to contain spherical particles, and comparison models assume non-spherical particles.

Figure 4. Tests of the ability to constrain non-spherical aerosols. (A) χ^2_{geom} for the same parameter space as in Figure 3, except that the measured and comparison models both assume non-spherical particles. (B) χ^2_{abs} for the same parameter space as in Figure 4A.

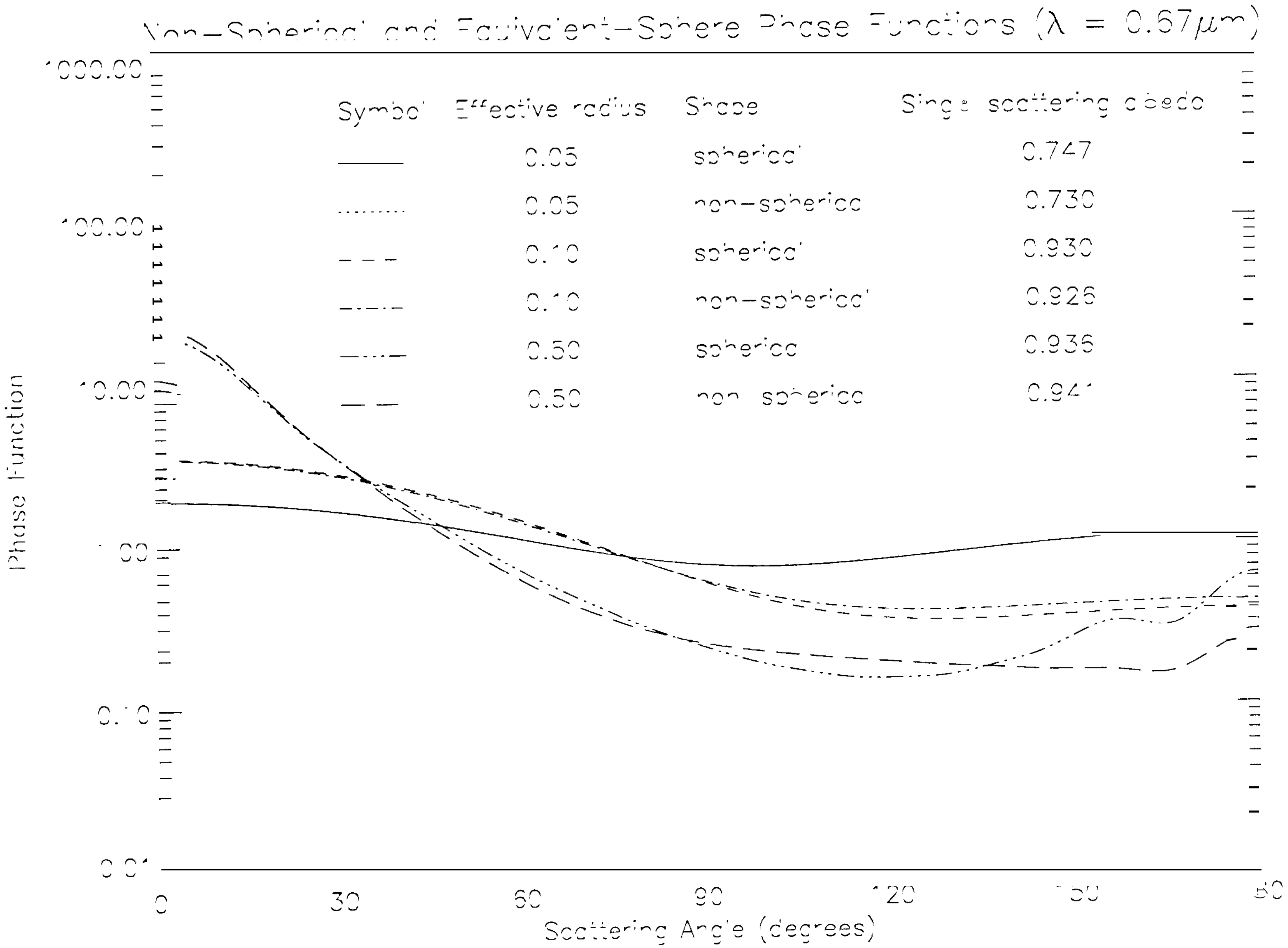

Non-Spherical and Equivalent-Sphere Phase Functions (λ = 0.67μm)
Symbol
Effective radius
Shape
Single scattering albedo
0.05
spherical
0.747
0.05
non-spherical
0.730
0.10
spherical
0.930
0.10
non-spherical
0.926
0.50
spherical
0.936
0.50
non spherical
0.941
1000.00
100.00
10.00
1.00
0.10
0.01
Phase Function
0
30
60
90
120
150
180
Scattering Angle (degrees)

FIGURE 1A

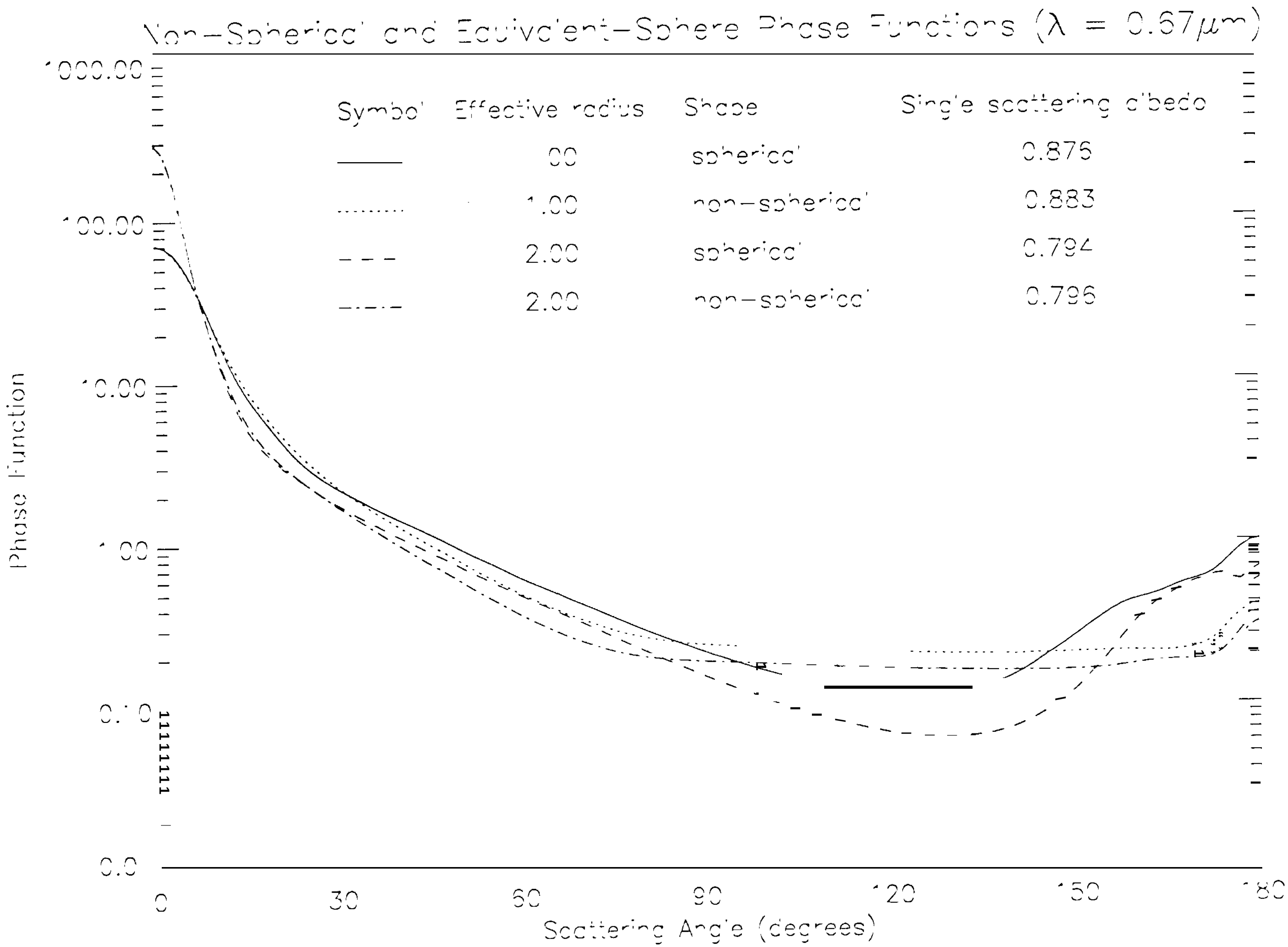
Non-Spherical and Equivalent-Sphere Phase Functions (λ = 0.67μm)
Symbol
Effective radius
Shape
Single scattering albedo
1.00
2.00
2.00
spherical
non-spherical
spherical
non-spherical
0.876
0.883
0.794
0.796
1000.00
100.00
10.00
1.00
0.10
0.0
Phase Function
0
30
60
90
120
150
180
Scattering Angle (degrees)

FIGURE 13

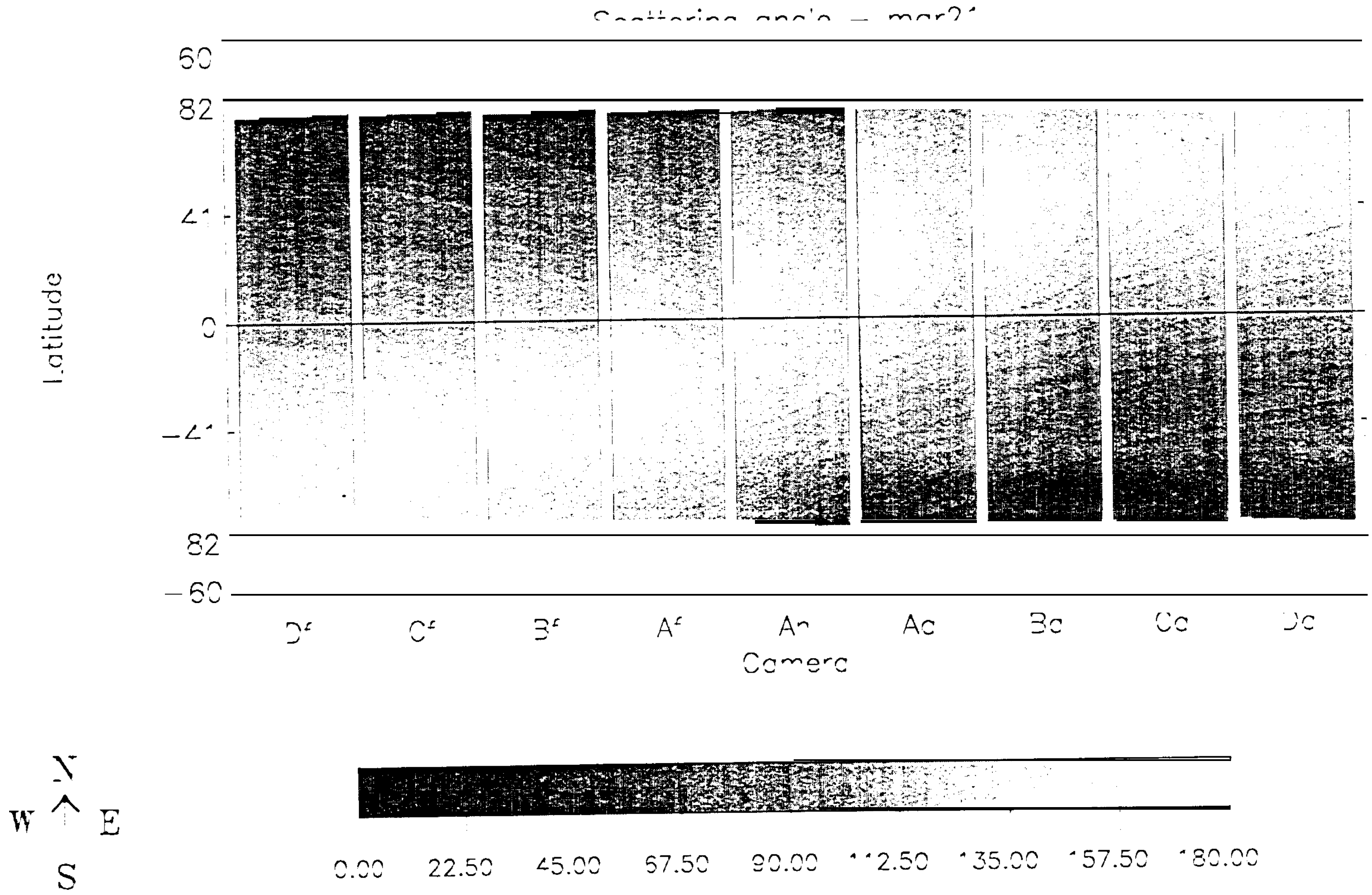

60
82
0
82
-60
Latitude
Camera
N
W
E
S
0.00
22.50
45.00
67.50
90.00
135.00
157.50

FIGURE 2

Non-Spherical Atmosphere, Spherical Comparison (Fresnel Surface)

μ_0 = 0.60 $\Delta\phi_{Nadir}$ = .26. 0

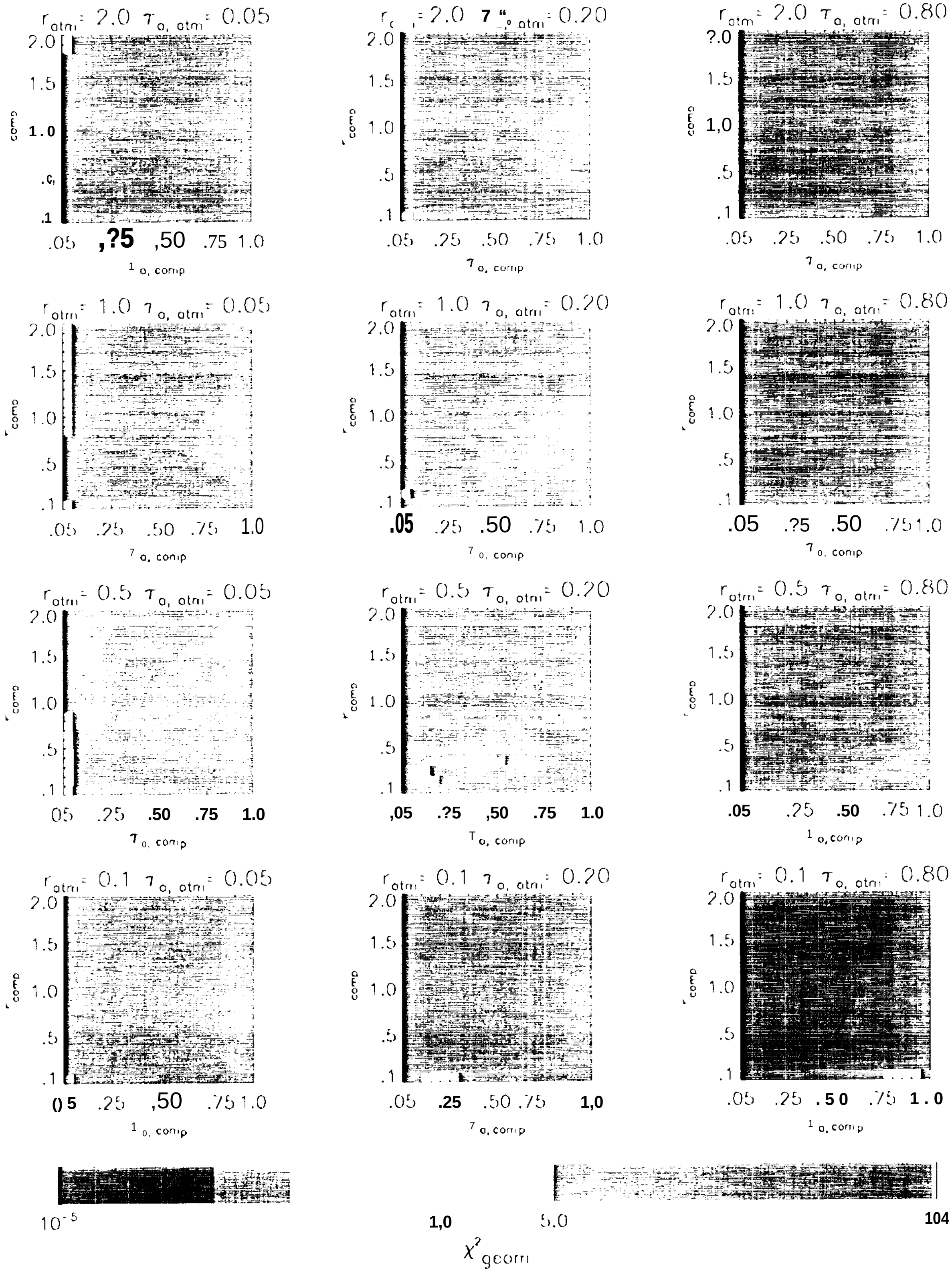

Fri Dec 8 15:46:55 1995

nonsp_sp_whisc_fresnel_reflectivity_12_95.dat

Spherical Atmosphere, Non- Spherical Comparison (Fresnel Surface)

μ_0 = 0.60 $\Delta\phi_{Nadir}$ = 26.0

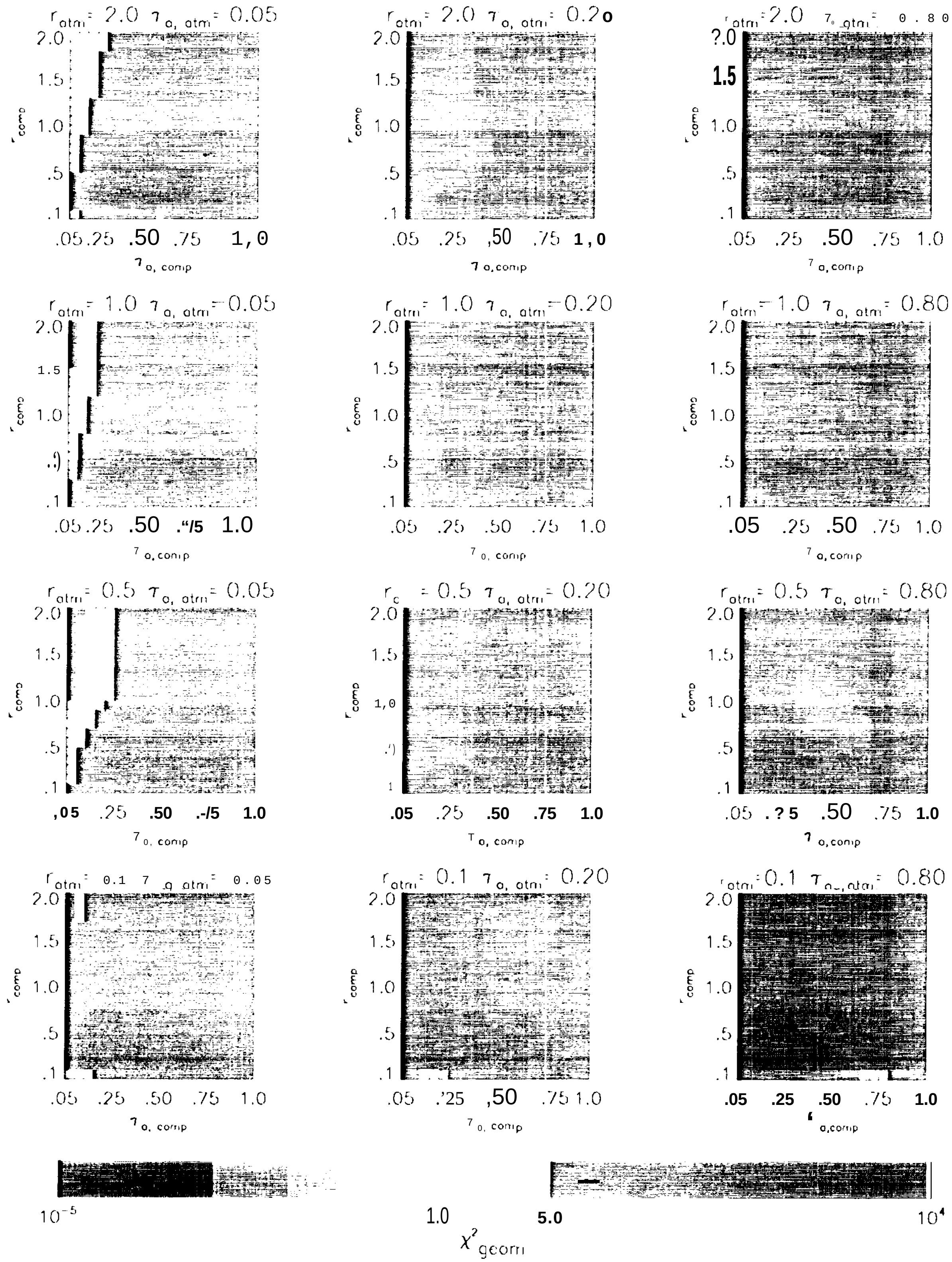

FIGURE 3B

Non- Spherical Atmosphere, Non- Spherical Comparison (Fresnel Surface)

$\mu_0 = 0.60 \quad \Delta\phi_{Nadir} = 26.0$

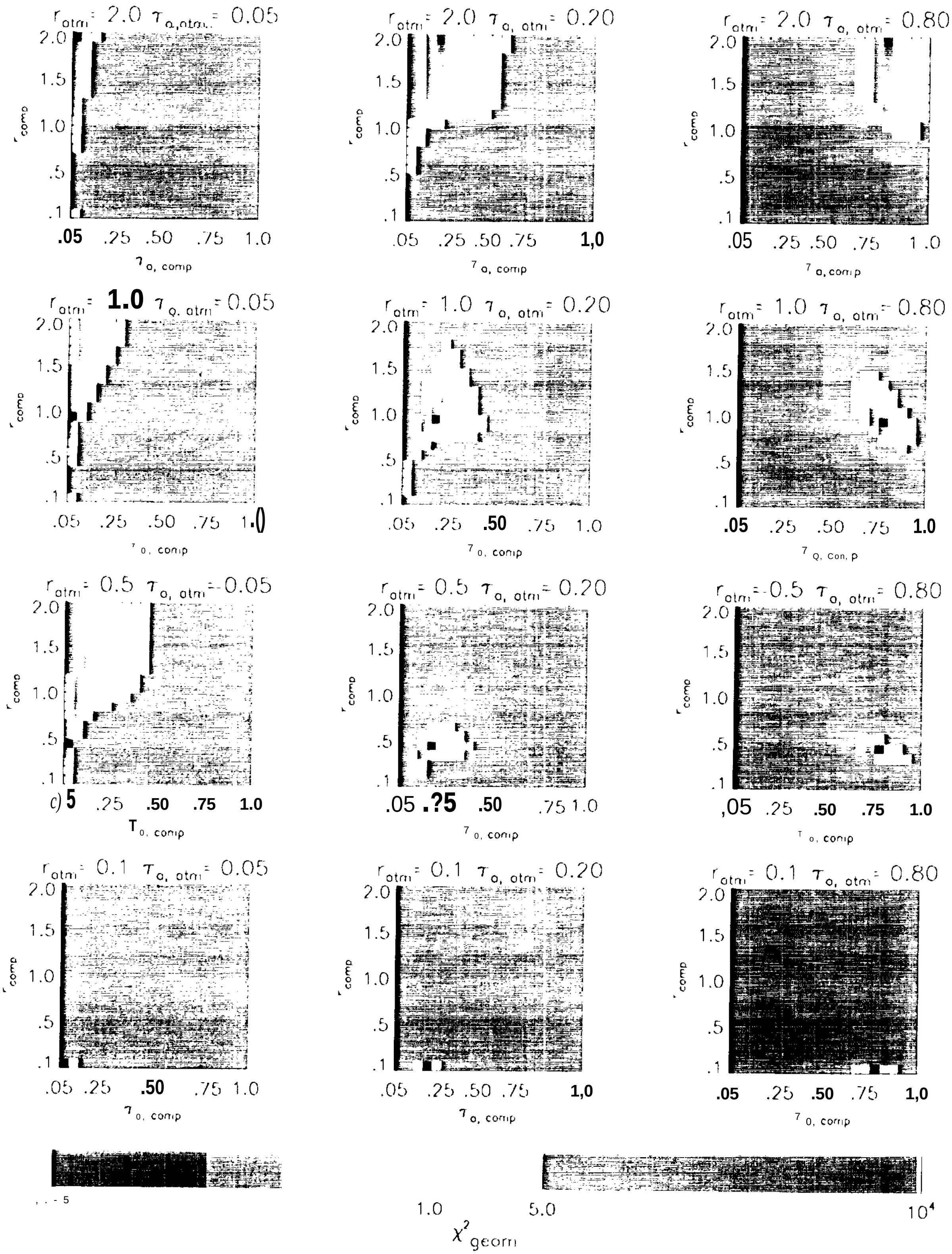

FIGURE 4A

Fri Dec 8 15:32:01 1995

nonsp_nonsp wchsci fresnel_var_reactivity_12_95.dat

Non Spherical Atmosphere, Non-Spherical Comparison (Fresnel Surface)

μ_0 = 0.60 $\Delta\phi_{Nadir}$ = 26.0

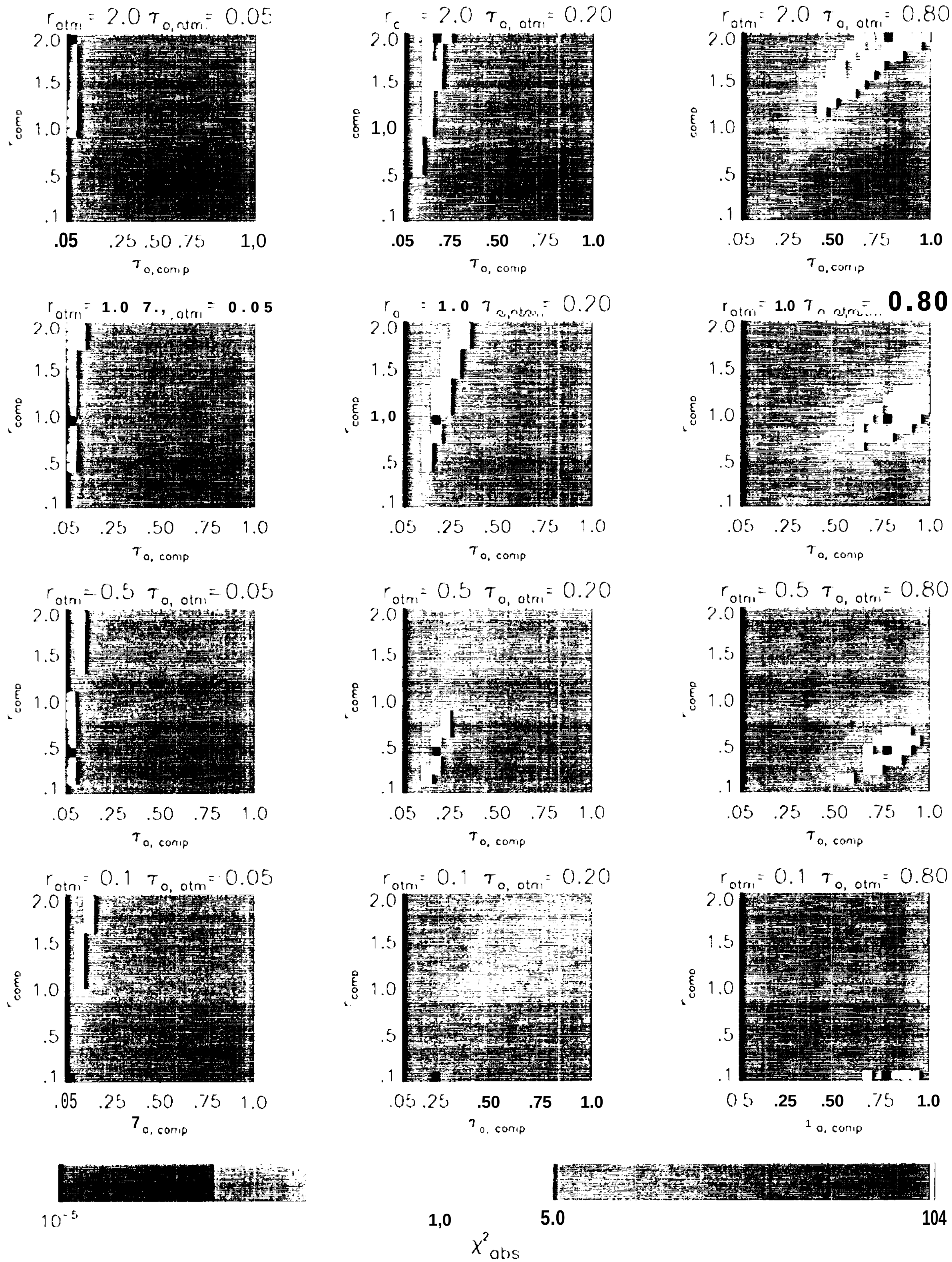

Fri Dec 8 15:3?:56 1995

nonsp_nonsp_wchisq_fresnel_vers ef?? c?vity. 12_95.dc?

FIGURE 4B